Tailoring porosity and rotational dynamics in a series of octacarboxylate metal-organic frameworks

Florian Moreau[a], Daniil I. Kolokolov[b,c], Alexander G. Stepanov[b,c], Timothy L. Easun[d], Anne Dailly[e], William Lewis[f], Alexander J. Blake[f], Harriott Nowell[g], Matthew J. Lennox[f], Elena Besley[f], Sihai Yang[a,1], and Martin Schröder[a,h,1]

[a]School of Chemistry, University of Manchester, Manchester M13 9PL, United Kingdom; [b]Boreskov Institute of Catalysis, Siberian Branch, Russian Academy of Sciences, Novosibirsk 630090, Russia; [c]Novosibirsk State University, Novosibirsk 630090, Russia; [d]School of Chemistry, Cardiff University, Cardiff CF10 3AT, United Kingdom; [e]Chemical and Environmental Sciences Laboratory, General Motors Corporation, Warren, MI 48090; [f]School of Chemistry, University of Nottingham, University Park, Nottingham NG7 2RD, United Kingdom; [g]Diamond Light Source, Oxon, OX11 0DE, United Kingdom; and [h]Nikolaev Institute of Inorganic Chemistry, Siberian Branch, Russian Academy of Sciences, Novosibirsk, 630090, Russia

Edited by Omar M. Yaghi, University of California, Berkeley/Lawrence Berkeley National Laboratory, Berkeley, CA, and accepted by Editorial Board Member Thomas E. Mallouk January 25, 2017 (received for review September 10, 2016)

Modulation and precise control of porosity of metal-organic frameworks (MOFs) is of critical importance to their materials function. Here we report modulation of porosity for a series of isoreticular octacarboxylate MOFs, denoted MFM-180 to MFM-185, via a strategy of selective elongation of metal-organic cages. Owing to the high ligand connectivity, these MOFs do not show interpenetration, and are robust structures that have permanent porosity. Interestingly, activated MFM-185a shows a high Brunauer–Emmett–Teller (BET) surface area of 4,734 m^2 g^{-1} for an octacarboxylate MOF. These MOFs show remarkable CH_4 and CO_2 adsorption properties, notably with simultaneously high gravimetric and volumetric deliverable CH_4 capacities of 0.24 g g^{-1} and 163 vol/vol (298 K, 5–65 bar) recorded for MFM-185a due to selective elongation of tubular cages. The dynamics of molecular rotors in deuterated MFM-180a-d_{16} and MFM-181a-d_{16} were investigated by variable-temperature ^2H solid-state NMR spectroscopy to reveal the reorientation mechanisms within these materials. Analysis of the flipping modes of the mobile phenyl groups, their rotational rates, and transition temperatures paves the way to controlling and understanding the role of molecular rotors through design of organic linkers within porous MOF materials.

metal-organic framework | copper | CO_2 | CH_4 | molecular rotors

Metal-organic frameworks (MOFs) are an emerging class of porous, multifunctional materials showing great potential in a wide range of applications (1–7). Given their metal-organic hybrid nature, MOFs have an exceptionally high degree of structural diversity and tailorability (8). Thus, not only is the on-demand design of materials that incorporate pores of precise shapes and dimensions achievable, but also the inner surface of these materials becomes a platform for incorporating desirable functionality for target applications (9, 10). Within the field of gas storage, there is a strong correlation between the material porosity and the maximum adsorption capacity. A common strategy to increase porosity in MOFs consists of targeting a framework topology and systematically elongating the linkers to generate additional pore space. This approach has shown success in a number of MOF systems, but is not without drawbacks. For example, increases in porosity typically correlate to increases in pore diameters, which can be detrimental to the strength of host–guest interactions at low surface coverage (11). Also, often simple ligand elongation will ultimately lead to framework interpenetration with reduced porosity and/or stability (12–14). A powerful driver therefore exists to find the ideal compromise between high porosity and strong host–guest interactions over a wide range of pressures.

The use of rigid, highly connected linkers (e.g., with 6–8 coordinating functions) affords potentially a more robust and stable platform for the development of isoreticular porous materials. This strategy has been widely implemented for $[Cu_2(O_2CR)_4]$ paddlewheel systems with hexacarboxylate linkers of C_3 symmetry to generate a family of ***rht***-type MOFs with high and predictable porosity (15–17). In contrast, effective modulation of porosity for isoreticular MOFs based upon 8-connected linkers has not been achieved to date (18–26), thus representing a significant synthetic challenge. We report herein modulation of porosity in a series of isoreticular octacarboxylate MOFs. By varying the length and nature of the heteropolyaromatic cores of the linkers on going from MFM-180 to MFM-185, we have selectively extended the length of metal-organic cages along one direction and also effectively avoided framework interpenetration. The resulting increase in porosity of the materials does not impair their stability toward activation, and the fixed diameter of the pores allows efficient packing of gas molecules across a wide range of pressures. The dynamics of molecular rotors (e.g., phenyl rings) within MOF materials is a key property to their functionalization as they form part of the internal pore surface and are thus highly sensitive to the presence of guest molecules (27–31). In this regard, the series of MOFs herein offer a unique platform to probe the influence of altering the ligand structure on the molecular dynamics and rotational freedom within the resultant framework. To the best of our knowledge, only a few attempts have been made to elucidate the rotational dynamics of linkers in porous MOFs (30–33) and none control them via linker design only. We report here the temperature-dependent ^2H NMR studies of selectively deuterated MFM-180-d_{16} and MFM-181-d_{16} to define the rotational and

Significance

A family of stable porous materials incorporating organic linkers and Cu(II) cations is reported. Their pores can be altered systematically by elongation of the ligands allowing a strategy of selective pore extension along one dimension. These materials show remarkable gas adsorption properties with high working capacities for CH_4 (0.24 g g^{-1}, 163 cm^3 cm^{-3} at 298 K, 5–65 bar) for the most porous system. The mechanism of rotation of the organic groups in the solid state has been analyzed by NMR spectroscopy and rotational rates and transition temperatures analyzed. Significantly, we show that framework dynamics can be controlled by ligand design only, and this paves the way to understanding the role of molecular rotors within these materials.

Author contributions: F.M., S.Y., and M.S. designed research; F.M., D.I.K., A.D., W.L., and A.J.B. performed research; A.G.S., A.D., A.J.B., H.N., M.J.L., and E.B. contributed new reagents/analytic tools; F.M., D.I.K., T.L.E., and S.Y. analyzed data; and F.M., D.I.K., A.G.S., T.L.E., A.D., W.L., A.J.B., H.N., M.J.L., E.B., S.Y., and M.S. wrote the paper.

The authors declare no conflict of interest.

This article is a PNAS Direct Submission. O.M.Y. is a Guest Editor invited by the Editorial Board.

Data deposition: The atomic coordinates and structure factors have been deposited in the Cambridge Structural Database, Cambridge Crystallographic Data Centre, www.ccdc.cam.ac.uk (accession codes CCDC 1472806–1472810.

[1]To whom correspondence may be addressed. Email: Sihai.Yang@manchester.ac.uk or M.Schroder@manchester.ac.uk.

This article contains supporting information online at www.pnas.org/lookup/suppl/doi:10.1073/pnas.1615172114/-/DCSupplemental.

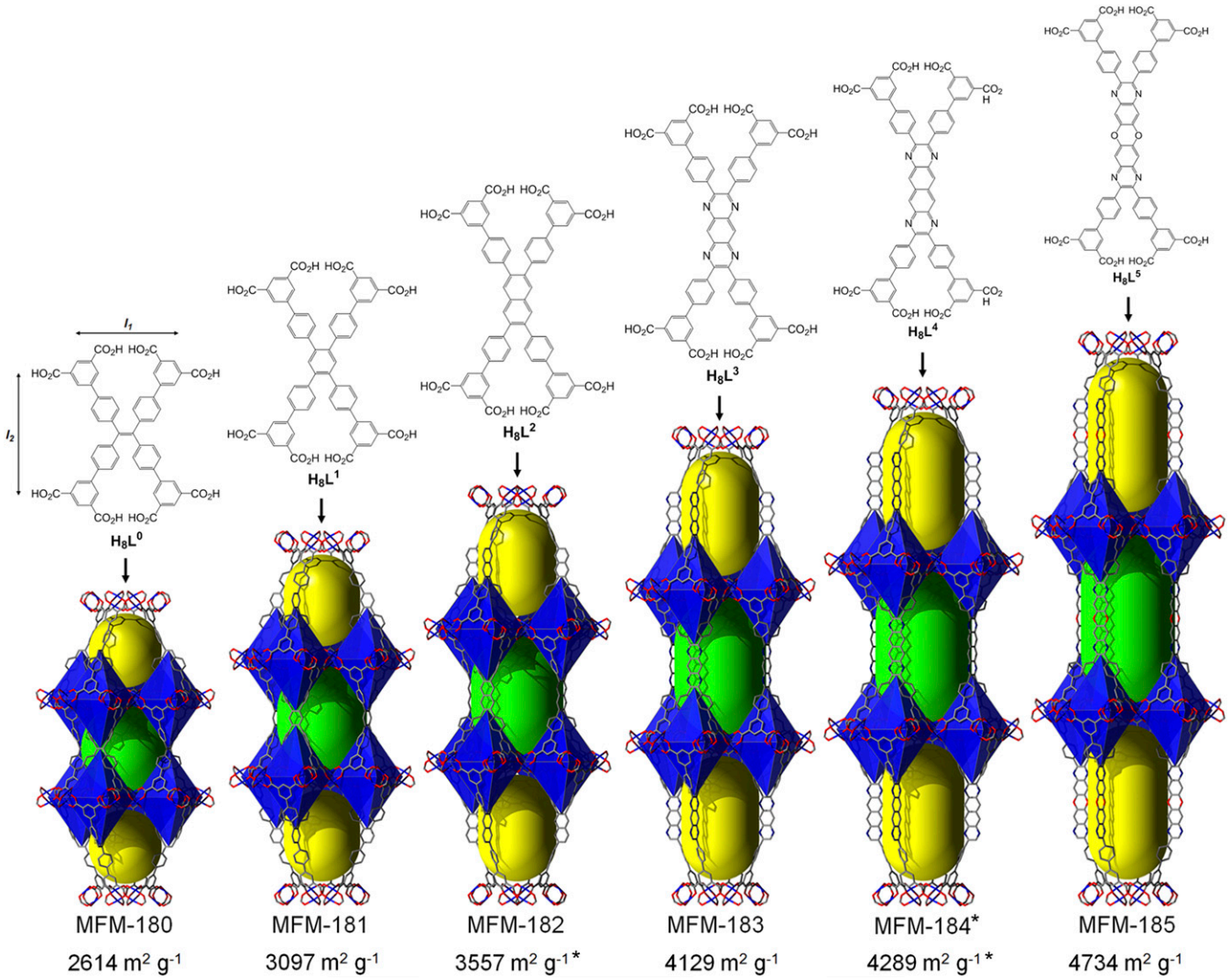

Fig. 1. Chemical structures for the octacarboxylate linkers H_8L^0 to H_8L^5 used for the synthesis of MFM-180 to MFM-185, representation of the cage assembly in MFM-180, MFM-181, MFM-182, MFM-183, MFM-184 (*predicted structure) and MFM-185, and corresponding BET surface areas (*computed).

flipping modes of the phenyl groups within these structures in the solid state and the molecular factors that govern these dynamics.

Results and Discussion

Design and Synthesis of Octaconnected Ligands and Isoreticular MOFs. The series of octaconnected linkers, ranging from 19 to 30 Å in dimension, are shown in Fig. 1 and their syntheses are described in detail in *SI Appendix*. H_8L^0, H_8L^3, and H_8L^5 were synthesized by direct Suzuki–Miyaura coupling of diethylisophthalate-5-boronic acid with the corresponding tetrahalides: 1,1,2,2-tetrakis(4-bromophenyl) ethane, 2,3,7,8-tetrakis(4-bromophenyl)pyrazino[2,3-*g*]quinoxaline, and 2,3,9,10-tetrakis(4-bromophenyl)-[1,4]dioxino[2,3-*g*:5,6-*g*′]diquinoxaline for H_8L^0, H_8L^3, and H_8L^5, respectively. In the case of H_8L^1 and H_8L^2, we used a different strategy where the extended 3′,5′-bis(ethoxycarbonyl)biphenyl-4-ylboronic acid was coupled with 1,2,4,5-tetrabromobenzene and 2,3,6,7-tetraiodonaphthalene, respectively. Attempts to prepare H_8L^4 from naphthalene-2,3,6,7-tetraamine failed, and therefore the target MOF MFM-184 was analyzed in silico based upon the isoreticular nature of this series of materials. Solvothermal reactions of H_8L^0, H_8L^1, H_8L^2, or H_8L^3 with $CuCl_2$ in a mixture of *N*,*N*′-diethylformamide/ethanol/0.1 M aqueous HCl (2/2/1, vol/vol/v) at 80 °C for 16 h afforded the solvated materials $[Cu_4(L^n)(H_2O)_4]_\infty$·solv or MFM-18n ($n$ = 0, 1, 2, 3). Due to the insolubility of H_8L^5 in the above solvent mixture, the synthesis of MFM-185 was conducted in a mixture of *N*,*N*′-dimethylformamide/DMSO/2 M aqueous HCl (40/20/1, vol/vol/v) with $Cu(NO_3)_2$0.2.5H_2O for 4 d. The "indirect" synthesis of $[Cu_4(L^0)(H_2O)_4]_\infty$ has been reported via transmetallation of the isostructural $[Zn_4(L(1))(H_2O)_4]_\infty$ complex, in which Zn(II) ions are gradually replaced by Cu(II) ions (24).

Analysis of the Crystal Structures. The X-ray single-crystal structures of MFM-180, -181, -182, -183, and -185, confirm the formation of square planar $[Cu_2(O_2CR)_4]$ nodes bridged by the octacarboxyate linkers to afford 3D open structures. MFM-180 crystallizes in the tetragonal space group $I\bar{4}2m$ with a = 18.6924(2) Å and c = 35.9196(4) Å. The octacarboxylate linker $[L^0]^{8-}$ comprises a central tetraphenylethylene core bearing four isophthalate moieties in 4,4′,4′′,4′′′ positions and acts as a 4-connected node (Fig. 1). Each isophthalate arm is orthogonal to the main plane of the molecule and acts as a 3-connected node. Each linker connects to eight $[Cu_2(O_2CR)_4]$ paddlewheels, and each paddlewheel connects to four independent linkers. As a result, the MFM-180 framework can be regarded as a 3,3,4-c ***tbo*** net (*SI Appendix*, Fig. S1) of stoichiometry $(3\text{-c})_4(4\text{-c})_3$ with the corresponding point symbol of $\{6^2{\cdot}8^2{\cdot}10^2\}_3\{6^3\}_4$ (34). The metal–ligand linkage affords

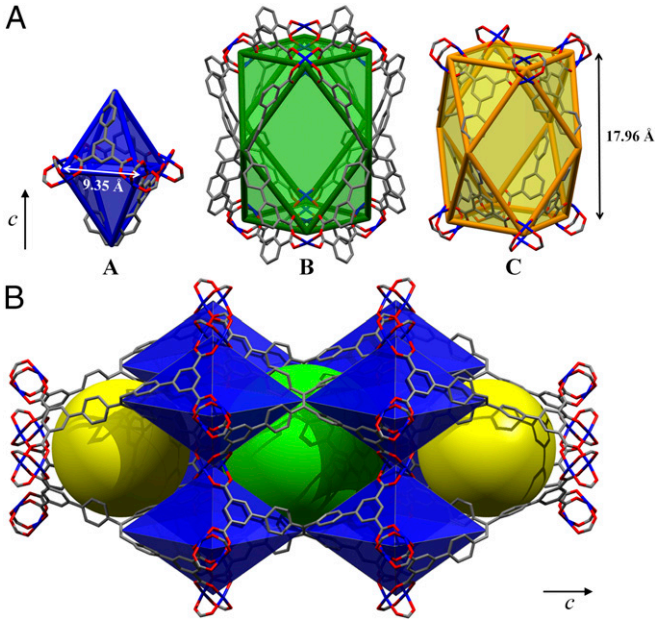

Fig. 2. View of (*A*) polyhedral representations of the three types of cages A (octahedral), B, and C (cuboctahedral) and (*B*) their 3D assembly in MFM-180.

three types of metal-organic cages (A, B, and C with a ratio of 2:1:1), the smallest of which is an elongated octahedral cage A comprising two ligands and four $[Cu_2(O_2CR)_4]$ paddlewheels (Fig. 2). The $[Cu_2(O_2CR)_4]$ moieties occupy the four equatorial vertices whereas two ethylene groups from the ligands occupy the apical vertices. The overall structure results from the corner-sharing assembly of these octahedral cages A via ethylene groups along the *c* axis and $[Cu_2(O_2CR)_4]$ paddlewheels along the *a*/*b* axis. This arrangement generates two types of elongated cuboctahedral cages, each one comprising four ligands and eight $[Cu_2(O_2CR)_4]$ paddlewheels (Fig. 2). The largest spheres that can fit within these cages taking into account the van der Waals radii of surface atoms have diameters of 3.0, 13.2, and 10.4 Å for cages A, B, and C, respectively. In cage B, the open metal sites of the paddlewheels point to the center of the cavity, whereas in cage C they are tangential to the cavity.

In previously reported examples of octacarboxylate MOFs with **tbo** or **scu** nets (18–26), the linkers present a central 4-connected node with increasing distances between the central node and four isophthalate moieties. Although this strategy produced isoreticular MOF structures, no increase of porosity was observed, presumably because of flexibility issues and/or highly strained frameworks. As an alternative approach to simply extending the linker length along all directions, we sought to target the extension of specific dimensionalities and lengths to better control the porosity of resultant MOFs. The distance l_1 (Fig. 1) is crucial for the formation of the octahedral cages A because it codes for the overall structural assembly. In contrast, the distance l_2 defines the length of cages B and C, and thus we sought to design linkers in which l_1 remains constant but l_2 is augmented. For this purpose, we replaced the 4-connected ethylene bond from the ligand H_8L^0 with a series of extended aromatic cores. The targeted isoreticular MOFs (except for MFM-184) were obtained as single crystals and their structures confirmed by single-crystal X-ray diffraction.

Replacement of the ethylenyl core in MFM-180 with a benzene ring affords MFM-181, which crystallizes in a different tetragonal space group *I*4/*mmm*. The change in space group is due to the presence of structural disorder in MFM-181, in which the free rotating phenyl rings are disordered over two positions generated by the mirror symmetry. Nonetheless, MFM-181 exhibits the same ***tbo*** topology as MFM-180 (*SI Appendix*, Fig. S1) when the phenyl core is considered as a 4-connected node. The octahedral cage A in MFM-181 is retained as expected. Cages B and C in MFM-181 are elongated along the *c* axis by 2.65 Å in comparison with MFM-180. The size of linkers $[L^2]^{8-}$, $[L^3]^{8-}$, and $[L^5]^{8-}$ is further increased by incorporating central cores with naphthalene, 3- and 5-fused heteroacenes, respectively. The corresponding MOFs, MFM-182, MFM-183, and MFM-185, all crystallize in the space group *I*4/*mmm* with the same type of cage assembly. Given the extension of the polyaromatic cores of $[L^2]^{8-}$, $[L^3]^{8-}$, and $[L^5]^{8-}$, the most accurate topological description of the underlying nets of MFM-182, MFM-183, and MFM-185 reflects a process called "decoration" in which a net vertex is replaced by a group of vertices. Thus, MFM-182, MFM-183, and MFM-185 present the same previously unreported 3,3,4-c net with point symbol $\{6.10^2\}\{6^2.8^2.10^2\}\{6^3\}_2$, which is derived from the **tbo** net by decoration of half of its 4-c vertices by a pair of 3-c vertices (*SI Appendix*, Fig. S1). The calculated accessible voids (PLATON) are 71.5%, 71.2%, 73.3%, 75.4%, and 76.7% for MFM-180, MFM-181, MFM-182, MFM-183, and MFM-185, respectively.

Modulation of Porosity and Gas Adsorption Property. Before activation (involving removal of both the free and coordinating solvents from the pores), the materials were exchanged with methanol. This was followed by heating the solvent-exchanged samples at 100 °C under dynamic vacuum to give activated MFM-180a and MFM-181a. To prepare activated MFM-183a and -185a, supercritical CO_2 drying was used to maximize the retention of their pore structure. MFM-180a, -181a, -183a, and 185a show Brunauer–Emmett–Teller (BET) surface areas of 2,610, 3,100, 4,130, and 4,730 $m^2\ g^{-1}$, respectively, as determined from N_2 adsorption at 77 K. The BET surface areas for MFM-182a and MFM-184a are predicted by grand canonical Monte Carlo methods to be 3,557 and 4,289 $m^2\ g^{-1}$, respectively, because of the difficulty in their bulk synthesis (*SI Appendix*). Analysis of the N_2 isotherms using a nonlocal density-functional theory model revealed the pore size distribution centered around 13.3, 13.7, 14.3, and 16.3 Å for MFM-180a, -181a, -183a, and 185a, respectively. Total pore volumes of 1.00, 1.36, 1.45, and 1.65 $cm^3\ g^{-1}$ were obtained from the N_2 isotherms, and compare favorably with those calculated based upon single crystal structure (1.09, 1.19, 1.40, and 1.59 $cm^3\ g^{-1}$ for MFM-180a, -181a, -183a, and -185a, respectively). Additionally, there is a good agreement between experimental and predicted BET surface areas (*SI Appendix*, Figs. S5–S18) and overall, the results confirm the complete activation of these MOFs and are consistent with the

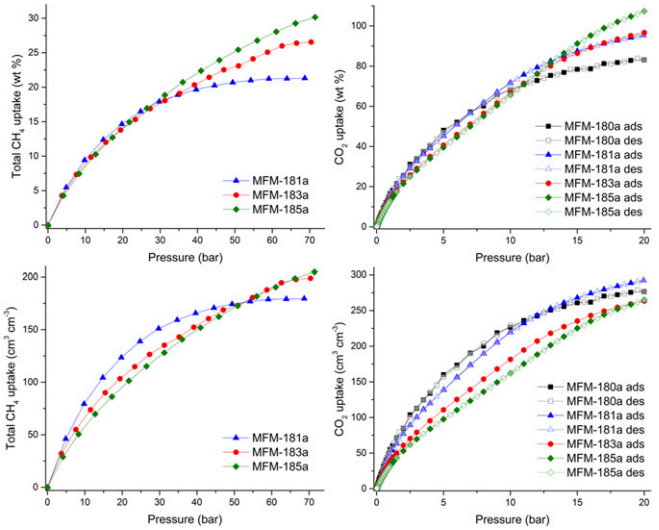

Fig. 3. High-pressure CH_4 sorption isotherms for MFM-181a, -183a, and -185a at 298 K and CO_2 sorption isotherms for MFM-180a, -181a, -183a, and -185a up to 20 bar at 298 K. (*Top*) gravimetric uptake; (*Bottom*) volumetric uptake.

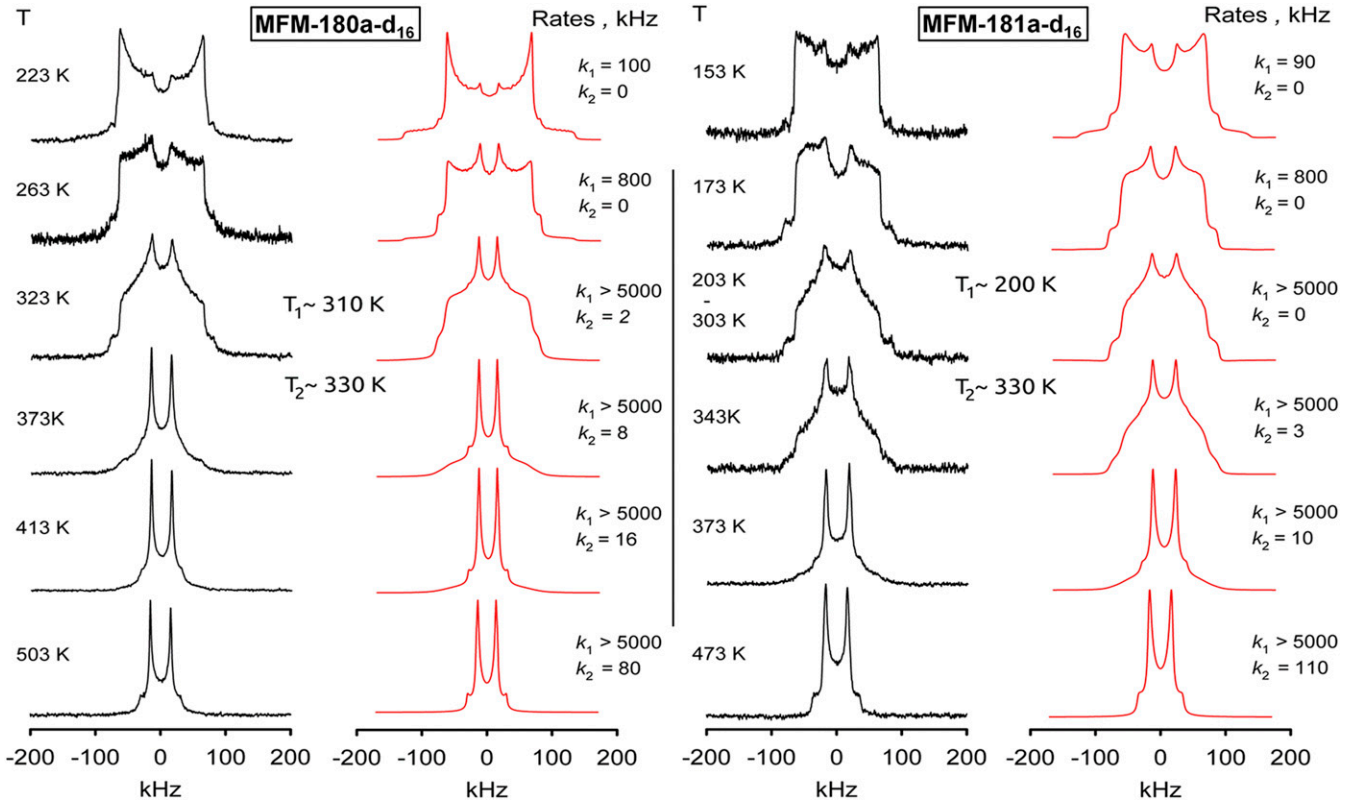

Fig. 4. Comparison of the ^{2}H NMR line shape temperature dependence for phenyl fragments in MFM-180a-d_{16} and MFM-181a-d_{16} (experimental, black; simulation, red).

increasing pore dimensions across the series. MFM-185a possesses one of the highest BET surface areas and pore volumes among octacarboxylate MOFs.

The CH_4 adsorption capacities of MFM-181a, -183a, and 185a are amongst the highest reported values for MOFs at 35 bar, 298 K (Fig. 3). Interestingly, the intrinsic trade-off between gravimetric and volumetric capacities is minimized in this series of MOFs owing to the high framework connectivity and thus relatively high crystal density in comparison with other highly porous MOFs. For example, both gravimetric and volumetric CH_4 adsorption capacities of MFM-181a, -183a, and 185a are higher than those reported for the highly porous octacarboxylate PCN-80a (17.7 wt %, 142 vol/vol) under the same conditions (1). CH_4 adsorption in MFM-181a is saturated at 55 bar, whereas MFM-183a and 185a can accommodate more CH_4 at higher pressures owing to their extended pore space. At 65 bar, the total gravimetric uptake of MFM-185a is sufficiently high (29.0 wt %) to compensate for its low crystal density and hence it displays the highest volumetric CH_4 uptake (198 vol/vol) of the series. Because MFM-181a, 183a, and 185a have almost identical CH_4 uptakes at 298 K and 5 bar, the desirable improvement in porosity through elongation of the metal-organic cages affords an increase in both gravimetric and volumetric "working capacities" (defined as the difference in total uptake between 65 and 5 bar). For example, MFM-185 shows high deliverable CH_4 capacity in both gravimetric and volumetric terms among octacarboxylate MOFs (*SI Appendix*, Table S6).

The CO_2 adsorption isotherms were recorded at 298 K up to 20 bar for MFM-180a, -181a, -183a, and 185a (Fig. 3). The isosteric heats of CO_2 adsorption were estimated to be ~23 kJ mol^{-1} for all MOFs (*SI Appendix*, Table S7). At low pressure (1 bar), both gravimetric and volumetric CO_2 uptakes are higher for the less porous frameworks, ranging from 13.0 wt % (32.2 vol/vol) for MFM-185a to 15.0 wt % (54.9 vol/vol) for MFM-180a, which suggests that a high density of open metal sites is crucial to maximize the low-pressure CO_2/framework interactions. For

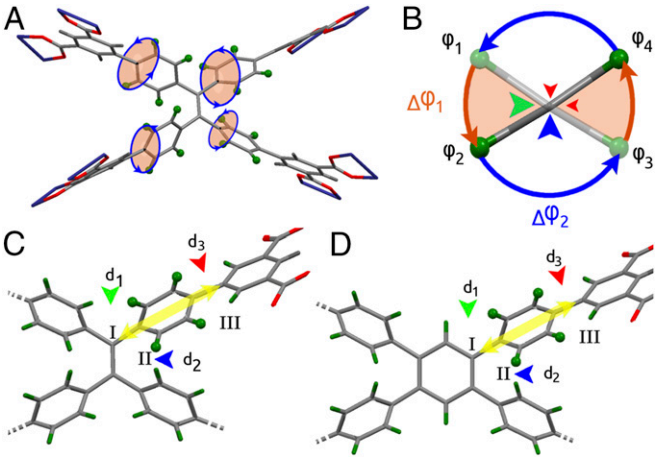

Fig. 5. (*A*) Representation of the linker in MFM-180a-d_{16} with its four mobile phenyl rings. (*B*) Scheme of rotation sites for phenyl groups in MFM-180a-d_{16} and MFM-181a-d_{16}. The reorientation scheme comprises a four-site exchange motion with two different rate constants: k_1 ($\Delta\varphi_1$) and k_2 ($\Delta\varphi_2$). The green arrow represents the barrier associated with k_1, the blue arrow represents the barrier associated with k_2, and the red arrows are associated with barriers in the $\Delta\varphi_1$ and $\Delta\varphi_2$ regions associated with minor steric restrictions. (*C* and *D*) Scheme of interaction sites that might influence the rotational potential for phenyl groups in MFM-180a-d_{16} and MFM-181a-d_{16}, respectively. Parameter d_2 is the shortest achievable distance for the electrostatic interaction between the phenyl hydrogens and is similar in both materials.

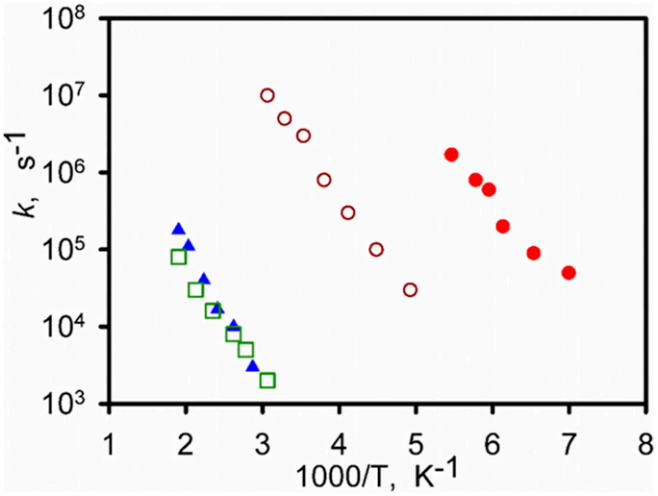

Fig. 6. Arrhenius plots of the rotational rate constants k : (○) k_1 and (□) k_2 for MFM-180a-d_{16}; (●) k_1 and (▲) k_2 for MFM-181a-d_{16}.

pressures higher than 10 bar, the larger pore volume of MFM-185a allows it to reach the highest gravimetric uptake (107.3 wt % at 20 bar) of the series whereas MFM-181a shows the highest volumetric CO_2 uptake (292.4 vol/vol at 20 bar) due to its combination of large surface area and moderately low density. These uptakes compare favorably with other octacarboxylate MOFs presenting higher (PCN-80a[25]: 72.8 wt % at 20 bar, 293 K) or similar (MFM-140[18]: 91.2 wt % at 20 bar, 298 K) porosities.

^{2}H NMR Studies on Dynamics of Molecular Rotors. Solid-state ^{2}H NMR spectroscopy was applied to investigate the molecular dynamics of the rotation of aromatic rings in this series of MOFs. MFM-180a and MFM-181a were partially deuterated by selectively introducing D atoms on the aromatic rings in the ligands to give MFM-180a-d_{16} and MFM-181a-d_{16} (*SI Appendix*). Variable-temperature ^{2}H NMR spectroscopic studies for MFM-180a-d_{16} and MFM-181a-d_{16} (see Fig. 4 and *SI Appendix* for full spectral data) show that the mobility of the phenyl groups for both materials evolves with temperature starting from a Pake-powder pattern with quadrupolar coupling parameters (Q_0 = 176 kHz, η = 0) typical for static phenyls C-D groups at low temperature (100 K). The evolution of the line shape with rising temperature depicts a reorientation mechanism similar for both MOFs with three regimes: (*i*) from low temperatures (100 K) up to T_1, the line shape evolves to a typical two-site exchange pattern (35); (*ii*) above T_1, the line shape remains stable up to T_2, and (*iii*) above T_2 it evolves to yield a narrowed uniaxial Pake pattern (Q_1 = 21 kHz ~ Q_0/8, η = 0), indicating that the phenyl fragments rotate homogeneously around the C_2 axis. Although the uniaxial ligand rotation in MOFs has been reported (30), the linkers in MFM-180a-d_{16} and MFM-181a-d_{16} show a more complex dynamic behavior.

The striking difference between MFM-180a-d_{16} and MFM-181a-d_{16} lies in the temperatures of transition from one motional mode to another, from two-site flipping to continuous rotation. For MFM-180a-d_{16}, T_1 is ~310 K and T_2 is ~330 K, whereas in MFM-181a-d_{16}, T_1 is ~200 K, and T_2 remains at 330 K. This result indicates that changes in the ligand core affect only one of the two rotational modes, with the flipping mode that evolves below T_1 being notably faster for MFM-181a-d_{16}. The line shape interpretation is based on the following general considerations. The position of mobile phenyl groups in the framework leaves freedom only for rotation or flipping about the C_2 axis and the angle between the rotation axis and the C–D bond is naturally fixed to be $\theta_{ph} = 60°$ (Fig. 5*A*). Therefore, the simplest model that can describe the line shape evolution is the four-site jump-exchange rotation for the torsional angle φ covering the whole 360° range (Fig. 5*B*). In such a scheme each of the two C–D bonds flips between two sites (φ_1 <> φ_2 and φ_3 <> φ_4) displaced by a jump angle $\Delta\varphi_1$. When the temperature conditions are met and the phenyl ring is able to overcome the second rotational barrier between the sites φ_1 <> φ_3 and φ_2 <> φ_4, each C–D bond begins to perform the full 360° rotation. In each pair only the highest barrier is relevant, and thus the motion can be described by the two independent rate constants k_1 and k_2. This model is evidenced by its excellent fit to the experimental data for both samples (Fig. 4). The two-site exchange motion governing the line shape below T_2 allows the determination of the exact position for C–D bond sites. For MFM-180a-d_{16}, the jump angle $\Delta\varphi_1^{I} = 71°$, whereas for MFM-181a-$d_{16}$, $\Delta\varphi_1^{II} = 68°$. The second jump angle can then be readily computed as $\Delta\varphi_2^{i} = 180° - \Delta\varphi_1^{i}$. This shows that the equilibrium positions are displaced compared with an ideal C_4 symmetry. The line shape evolution above T_2 fully supports the four sites exchange model and excludes any other interpretation of the observed spectra. Most intriguing are the potential barriers and collision factors involved. In all cases, the rotation rates follow the standard Arrhenius law (Fig. 6). For k_1 in MFM-180a-d_{16} the parameters are E_1 = 26 kJ mol^{-1} and $k_{10} = 1.6 \times 10^{11}$ Hz, and for MFM-181a-d_{16} E_1 = 20 kJ mol^{-1} and $k_{10} = 9 \times 10^{11}$ Hz. For k_2 in MFM-180a-d_{16} E_2 = 28 kJ mol^{-1} and $k_{20} = 3 \times 10^7$ Hz, whereas for MFM-181-d_{16} E_2 = 34 kJ mol^{-1} and $k_{20} = 4.6 \times 10^8$ Hz. Additional analysis suggests that intramolecular steric interactions in MFM-180a-d_{16} are stronger. In both cases these interactions are maximized when all phenyls lie in one plane, with three interaction sites and H–D or D–D distances governing the strength of interaction (Fig. 5 *C* and *D*). For MFM-180a-d_{16} site I shows the interaction of two mobile phenyl groups in 1,1′ positions of the ethylene core, whereas for MFM-181a-d_{16} it is the interaction of the mobile fragment with the hydrogen of the aromatic core fragment. Sites II and III are geometrically similar for both materials and the shortest distance is realized for site II (marked blue in Fig. 5 *C* and *D*). The rates of the slowest motion k_2 (Fig. 6) are almost superimposable for both frameworks and we can thus attribute k_2 to the torsional barrier that rises from electrostatic interaction between neighboring hydrogens in site II. Hence the rate constant k_1 must be governed by site I because the shortest possible distance at the site III is d_3 ~1.9 Å and is identical in the two linkers, whereas for site I for MFM-180a-d_{16} d_1 ~1.6 Å and for the MFM-181a-d_{16} d_1 ~1.9 Å. The comparison of the first motion rates k_1 for the two materials confirms that they are indeed considerably different: k_1 is much greater in MFM-181-d_{16} than in MFM-180-d_{16}. Interestingly, whereas the flipping mode k_1 in both cases is characterized by a collision factor typical for flipping motion in MOFs ~10^{11} Hz (30, 33), for k_2 it is ~3 orders of magnitude smaller at ~10^8 Hz, which reflects the strong influence of the steric restrictions on the axial rotation of the phenyl groups in these linkers. This ^{2}H NMR study has revealed that the complex dynamic behavior of the molecular rotors in MOFs in solid state can be elucidated and thus controlled by establishing a strong correlation between the ligand design and the rotational dynamics, the latter of which is a key property of MOF functionalities.

Conclusion

A series of isoreticular MOF materials based on a family of octacarboxylate linkers has been developed. The rigid, heteropolyaromatic linkers were designed to self-assemble with $[Cu_2(O_2CR)_4]$ paddlewheels to afford frameworks with elongated nanotubular cages of fixed diameter. The isoreticular design results in systematically increased pore volumes and surface areas for the MOFs. Notably, in the case of CH_4 adsorption, extension of the linker causes no uptake loss in the low-pressure region, and both gravimetric and volumetric uptakes are simultaneously

enhanced at high pressure. This affords an impressive CH_4 working capacity of 0.24 g g^{-1} and 163 vol/vol (298 K, 5–65 bar) for activated MFM-185a. We attribute this behavior to the efficient packing of gas molecules in the tubular pores and the high connectivity (and thus suitably high crystal density) of the framework. In addition, a rational synthetic design has allowed control of the torsional dynamics of linkers in MOF solids. The high predictability of the linker/metal self-assembly combined with their pore shape make this series of MOFs a unique platform for exploring further the tuning of porosity, decoration of pores, and development and control of new molecular rotors in functional MOFs.

Materials and Methods

The ligands H_8L^0, H_8L^1, H_8L^2, H_8L^3, and H_8L^5 were synthesized using a Suzuki–Miyaura coupling reaction between the corresponding tetrahalogenated core and boronic acid, followed by hydrolysis of the ester functions. The synthesis of H_8L^1 is described in detail in *SI Appendix*. The selectively deuterated linkers were synthesized following the same procedures but starting from deuterated building blocks.

Synthesis of MFM-180, -181, -182, and -183: H_8L^{0-3} (0.30 mmol) and $CuCl_2$ (0.19 g, 1.40 mmol) was dissolved in N,N′-diethylformamide (30 mL). EtOH (30 mL) and an aqueous solution of HCl (0.1M, 15 mL) were added to the resulting solution, which was placed in a tightly capped 250 mL Duran pressure plus laboratory bottle (cat. no. 1092234). The solution was heated at 80 °C in an oven for 16 h, and a large amount of crystalline product precipitated. The crystal plates of the corresponding MOF were isolated by filtration while the mother liquor was still warm.

Due to the poor solubility of H_8L^5, MFM-185 was synthesized following slightly different conditions (*SI Appendix*).

Detailed synthesis procedures and characterizations of the linkers and MOFs, along with crystallographic data and description of gas sorption and solid-state ^2H NMR experiments can be found in *SI Appendix*.

CCDC 1472806–1472810 contain the supporting crystallographic data for materials MFM-180, -181, -182, -183, and -185, respectively. These data can be obtained free of charge from the Cambridge Crystallographic Data Centre via https://www.ccdc.cam.ac.uk/structures-beta/. Please also see Datasets S1–S5 for materials MFM-180, -181, -182, -183, and -185.

ACKNOWLEDGMENTS. We thank the Engineering and Physical Sciences Research Council UK (Grant EP/I011870), the University of Nottingham, and the University of Manchester for funding. M.S. gratefully acknowledges receipt of European Research Council Advanced Grant AdG 226593 and acknowledges the Russian Ministry of Science and Education for the award of Russian Megagrant 14.Z50.31.0006. M.S. and D.I.K. gratefully acknowledge receipt of the Royal Society International Exchanges Scheme Grant Reference IE150114. E.B. acknowledges receipt of European Research Council Consolidator Grant 307755 FIN. We acknowledge the High Performance Computing (HPC) Facility at the University of Nottingham for providing computational time. T.L.E. gratefully acknowledges receipt of a Royal Society University Research Fellowship. We thank Diamond Light Source for access to beamline I19.

1. He Y, Zhou W, Qian G, Chen B (2014) Methane storage in metal-organic frameworks. *Chem Soc Rev* 43(16):5657–5678.
2. Zhang Z, Yao Z, Xiang S, Chen B (2014) Perspective of microporous metal–organic frameworks for CO2 capture and separation. *Energy Environ Sci* 7:2868.
3. Yang S, et al. (2012) Selectivity and direct visualization of carbon dioxide and sulfur dioxide in a decorated porous host. *Nat Chem* 4(11):887–894.
4. Horcajada P, et al. (2012) Metal-organic frameworks in biomedicine. *Chem Rev* 112(2):1232–1268.
5. Lee J, et al. (2009) Metal-organic framework materials as catalysts. *Chem Soc Rev* 38(5):1450–1459.
6. Li JR, Sculley J, Zhou HC (2012) Metal-organic frameworks for separations. *Chem Rev* 112(2):869–932.
7. Mondloch JE, et al. (2015) Destruction of chemical warfare agents using metal-organic frameworks. *Nat Mater* 14(5):512–516.
8. Li M, Li D, O'Keeffe M, Yaghi OM (2014) Topological analysis of metal-organic frameworks with polytopic linkers and/or multiple building units and the minimal transitivity principle. *Chem Rev* 114(2):1343–1370.
9. Alsmail NH, et al. (2014) Analysis of high and selective uptake of CO2 in an oxamide-containing Cu2(OOCR)4-based metal-organic framework. *Chemistry* 20(24):7317–7324.
10. Yang S, et al. (2014) Supramolecular binding and separation of hydrocarbons within a functionalized porous metal-organic framework. *Nat Chem* 7(2):121–129.
11. Lin X, Champness NR, Schröder M (2010) Hydrogen, methane and carbon dioxide adsorption in metal-organic framework materials. *Top Curr Chem* 293:35–76.
12. Batten S, Robson R (1998) Interpenetrating nets: Ordered, periodic entanglement. *Angew Chem Int Ed* 37:1460–1494.
13. Haldar R, Sikdar N, Maji T (2015) Interpenetration in coordination polymers: Structural diversities toward porous functional materials. *Mater Today* 18:97–116.
14. Lin X, et al. (2009) High capacity hydrogen adsorption in Cu(II) tetracarboxylate framework materials: The role of pore size, ligand functionalization, and exposed metal sites. *J Am Chem Soc* 131(6):2159–2171.
15. Yan Y, et al. (2009) Exceptionally high H2 storage by a metal–organic polyhedral framework. *Chem Commun* (9):1025–1027.
16. Nouar F, et al. (2008) Supermolecular building blocks (SBBs) for the design and synthesis of highly porous metal-organic frameworks. *J Am Chem Soc* 130(6):1833–1835.
17. Farha OK, et al. (2012) Metal-organic framework materials with ultrahigh surface areas: Is the sky the limit? *J Am Chem Soc* 134(36):15016–15021.
18. Tan C, et al. (2011) High capacity gas storage by a 4,8-connected metal-organic polyhedral framework. *Chem Commun (Camb)* 47(15):4487–4489.
19. Ma L, Mihalcik DJ, Lin W (2009) Highly porous and robust 4,8-connected metal-organic frameworks for hydrogen storage. *J Am Chem Soc* 131(13):4610–4612.
20. Mihalcik DJ, Zhang T, Ma L, Lin W (2012) Highly porous 4,8-connected metal-organic frameworks: Synthesis, characterization, and hydrogen uptake. *Inorg Chem* 51(4):2503–2508.
21. Eubank JF, et al. (2011) The quest for modular nanocages: tbo-MOF as an archetype for mutual substitution, functionalization, and expansion of quadrangular pillar building blocks. *J Am Chem Soc* 133(36):14204–14207.
22. Xue Y, et al. (2012) Structural diversity and properties of coordination polymers built from a rigid octadentenate carboxylic acid. *Cryst Growth Des* 12:6158–6164.
23. Zhuang W, et al. (2012) Robust metal–organic framework with an octatopic ligand for gas adsorption and separation: Combined characterization by experiments and molecular simulation. *Chem Mater* 24:18–25.
24. Wei Z, Lu W, Jiang HL, Zhou HC (2013) A route to metal-organic frameworks through framework templating. *Inorg Chem* 52(3):1164–1166.
25. Lu W, Yuan D, Makal TA, Li JR, Zhou HC (2012) A highly porous and robust (3,3,4)-connected metal-organic framework assembled with a 90° bridging-angle embedded octacarboxylate ligand. *Angew Chem Int Ed Engl* 51(7):1580–1584.
26. Spanopoulos I, et al. (2016) Reticular synthesis of HKUST-like tbo-MOFs with enhanced CH4 storage. *J Am Chem Soc* 138(5):1568–1574.
27. Kolokolov DI, et al. (2010) Dynamics of benzene rings in MIL-53(Cr) and MIL-47(V) frameworks studied by 2H NMR spectroscopy. *Angew Chem Int Ed Engl* 49(28):4791–4794.
28. Gould SL, Tranchemontagne D, Yaghi OM, Garcia-Garibay MA (2008) Amphidynamic character of crystalline MOF-5: Rotational dynamics of terephthalate phenylenes in a free-volume, sterically unhindered environment. *J Am Chem Soc* 130(11):3246–3247.
29. Kolokolov D, Stepanov A, Jobic H (2014) Guest controlled rotational dynamics of terephthalate phenylenes in metal–organic framework MIL-53(Al): Effect of different xylene loadings. *J Phys Chem C* 118:15978–15984.
30. Horike S, et al. (2006) Dynamic motion of building blocks in porous coordination polymers. *Angew Chem Int Ed Engl* 45(43):7226–7230.
31. Comotti A, Bracco S, Ben T, Qiu S, Sozzani P (2014) Molecular rotors in porous organic frameworks. *Angew Chem Int Ed Engl* 53(4):1043–1047.
32. Inukai M, et al. (2015) Control of molecular rotor rotational frequencies in porous coordination polymers using a solid-solution approach. *J Am Chem Soc* 137(38):12183–12186.
33. Comotti A, Bracco S, Sozzani P (2016) Molecular rotors built in porous materials. *Acc Chem Res* 49(9):1701–1710.
34. Delgado-Friedrichs O, O'Keeffe M, Yaghi OM (2006) Three-periodic nets and tilings: Edge-transitive binodal structures. *Acta Crystallogr A* 62(Pt 5):350–355.
35. Macho V, Brombacher L, Spiess H (2001) The NMR-WEBLAB: An internet approach to NMR lineshape analysis. *Appl Magn Reson* 20:405–432.